RESEARCH

Structural, Morphological, Optical and Dielectric Properties of Ternary PANI–ZnO–PPy Nanocomposite for Optoelectronic Applications

Priyanka Elumalai[1] · Julie Charles[1] · Satheesh Kumar Gopal[2]

Abstract

The ternary nanocomposite PANI–ZnO–PPy, which is composed of polyaniline (PANI), zinc oxide (ZnO) and polypyrrole (PPy) was effectively synthesized by in situ chemical oxidative polymerization technique using suitable oxidants to initiate the polymerization process in the monomers. The synthesized unary ZnO and ternary PANI–ZnO–PPy were characterized through various physico-chemical techniques. The semicrystalline nature and effective encapsulation of ZnO nanoparticles into the binary PANI–PPy matrix of PANI–ZnO–PPy was confirmed through XRD and FESEM analysis. The prominent vibrational bands of the functional groups present in ZnO and PANI–ZnO–PPy were detected through FTIR. The optical band gap value of ternary PANI–ZnO–PPy was found to be low compared to ZnO nanoparticles. Further, the dielectric properties and AC conductivity of binary matrix and ternary nanocomposite were investigated in the frequency range of 1 kHz to 1 MHz at room temperature. To ascertain the suitability of the materials in optoelectronic devices, the dielectric and conductivity studies were also analyzed in the temperature range of 30 °C to 150 °C. The studies revealed high dielectric constant and improved electrical conductivity of as-prepared PANI–ZnO–PPy nanocomposite compared to PANI–PPy matrix. From TGA, the substantial thermal stability exhibited by the synthesized ternary material further confirmed its high suitability for electronic device applications.

Keywords PANI–ZnO–PPy · Optical band gap · Dielectric constant · Dielectric loss · Tangent loss · Electric modulus

1 Introduction

In recent past, development of sustainable optoelectronic devices have gained massive attraction due to their applicability in multiple domains, not limiting to automatic control systems, power electronics, telecommunications, energy storage, military services and medical instruments. The miniaturization of optoelectronics devices has also offered incredible performance gain in many such applications. It is because the device performance increases as the volume of the optoelectronic material decreases, hence improving the speed of operation, signal-to-noise ratio and quantum efficiency. Also, miniaturization of devices adds to benefits like cost effectiveness, ease of fabrication and fine optical

properties [1]. The use of conventional materials as components to optoelectronic devices is not considered beneficial due to their high production cost and complex processing techniques in large area applications. Subsequently, organic conducting polymer based optoelectronic devices are gaining more attention nowadays as they are more flexible, light weight, cost effective and are simple to process. However, conducting polymer based devices are less efficient than the conventional types and their weak stability can lead to device failure at a temperature slightly higher than ambient temperature. This problem can be resolved by incorporating the suitable reinforcements/fillers into conductive polymer materials to form conducting polymer composites or hybrids. The filler and the polymer matrix work together by complimenting each other's properties in order to improve the interfacial interaction between them. This leads to the resultant conducting polymer composites with improved electrical, optical, structural and thermal properties, which when used as an active material in electronic or optoelectronic devices can increase the device-lifetime.

✉ Julie Charles
  juliecharles@ssn.edu.in

1   Department of Physics, Sri Sivasubramaniya Nadar College of Engineering, Kalavakkam 603110, India

2   Department of Mechanical Engineering, Sri Sivasubramaniya Nadar College of Engineering, Kalavakkam 603110, India

In general, conducting polymer based nanocomposites are mainly divided into three categories, namely, polymer/ceramic, polymer/metal oxide and polymer/layered silicate. Among these, polymer/metal oxide combination plays an important role in optoelectronic devices owing to their interesting features like high electrical and optical conductivity, increased thermal and structural stability, high electrical permittivity, biocompatibility, good environmental stability, multiple oxidation states and fast doping/dedoping rate. These characteristics make conducting polymer-based nanocomposites the most promising choices for optoelectronic devices, light emitting diodes, photodetectors, electrochemical sensors, field effect transistors, stretchable electronics, supercapacitors, solar cells, lithium-ion batteries, transistors and printed electronics applications [2, 3]. Amidst the various conducting polymers [4–10], PANI and PPy are chosen as prominent materials for optoelectronic devices owing to the exhibition of high electron affinity and enhanced electrical conductivity. Also, their low ionization potential and the requirement for minimum energy threshold for the occurrence of optical transitions, eco-friendliness and low synthesis cost adds on to the merits [11]. Despite these attractive features, both PANI and PPy have some demerits because of their poor sensitivity, inferior thermal and mechanical properties and low processability. Hence, the present research work is oriented towards the enhancement of thermal, optical, electrical and dielectric aspects of PANI and PPy polymers through the inclusion of ZnO into the binary matrix. The idea of encapsulation of nanoscale ZnO within the binary conducting polymeric network is to increase the interfacial interaction between individual components in the ternary polymeric PANI–ZnO–PPy nanocomposite. By this way, PANI, ZnO and PPy could complement each other in a number of ways leading to improved physicochemical characteristics of the ternary nanocomposite.

The characteristic of conducting polymer nanocomposites depends upon various parameters such as structure, filler dimension, nanofiller concentration and synthesis route. Among these factors, the selection of synthesis technique and the type and concentration of filler plays a predominant role as they decide the desired nanocomposite properties. Several one pot (in situ) and two pot (ex situ) approaches are available to synthesize conducting polymer nanocomposites including sol gel, hydrothermal, electrochemical deposition, polymerization, coprecipitation and melt mixing [12]. Amidst these techniques, one pot (in situ) polymerization is the frequently used synthesis method to prepare the polymer nanocomposites because it provides several benefits, namely ease of synthesis, affordability and results in homogeneous state with boosted optoelectronic properties. It is well-known that some of the high k-dielectric constant metal oxides like ZnO, TiO_2, CeO_2, Al_2O_3, Ta_2O_5, ZrO_2 and SiO_2 [13–20] are used as nanofillers to the conducting polymer based materials. Amongst the mentioned inorganic metal oxides, zinc oxide (ZnO), being a n-type semiconductor, is very appropriate for optical and optoelectronic applications. It is due to the exhibition of direct band gap (3.37 eV) energy, strong adsorption ability and high dielectric permittivity of zinc oxide. ZnO nanostructured materials have many potential applications like transparent electrode in solar cells, chemical and gas sensor, spintronic device and impedance spectroscopy. Currently, there are only few research reports on the polymer based nanocomposites and metal-oxide reinforced polymeric materials for optoelectronic applications. For instance; Ajeet Verma et al. reported the synthesis of PANI–PPy–CdS nanocomposite by oxidative polymerization technique that exhibited high electron–hole recombination rate, high dielectric constant with low dielectric loss at 363 K. The resultant nanocomposite was used as electron transport layer for OLED applications [21]. Chakradhar et al. explored the impedance and dielectric behavior of PANI/V_2O_5 nanocomposite using single step in situ polymerization process by varying the weight percentage of V_2O_5 in PANI matrix. As a result, the binary nanocomposite exhibited a high ac conductivity value of 2.6×10^{-3} Scm^{-1} while loading 40% of nanofiller V_2O_5 in polyaniline matrix [22]. Priyanka et al. synthesized ternary PANI–PPy–NiO composite effectively by employing in situ polymerization route and examined its optical characteristics for its suitability in optoelectronic devices [23]. Vishnuvardhan et al. synthesized binary PPy/Y_2O_3 nanocomposite, which showed higher dielectric constant and electrical conductivity for 30% weight percentage of Y_2O_3 in polypyrrole matrix [24]. Safenaz and coworkers [25] developed a binary nanocomposite comprised of polyaniline (PANI) and silver nanoparticles that was again prepared by chemical oxidative polymerization. According to the results, the binary PANI/Ag revealed a significant enhancement of dielectric characteristics and electrical conductivity in comparison to pure PANI. Till date, synthesis of ternary PANI–ZnO–PPy nanocomposite and its analysis to validate its suitability for optoelectronic device applications has not been explored yet.

In the current research work, the report on the synthesis and characterization of ternary (PANI–ZnO–PPy) nanocomposite for optoelectronic device applications is made. The investigations on the structure, phase, morphology, optical activity and thermal of PANI–ZnO–PPy nanocomposite was carried out using various physicochemical techniques such as X-ray powder diffraction (XRD), Field emission Scanning electron microscopy (FESEM), Energy-dispersive X-ray spectroscopy (EDAX), Fourier-transform infrared spectroscopy (FTIR), Thermogravimetric analysis (TGA) and Ultraviolet–visible spectroscopy (UV–Vis). From Tauc's plot, the calculated band gap value was found to be lower in PANI–ZnO–PPy nanocomposite when compared to ZnO nanoparticles, indicating favourable opto-electrical

properties of the ternary nanocomposite. To ascertain this, the dielectric and electrical analysis of binary (PANI–PPy) and ternary (PANI–ZnO–PPy) nanocomposites were carried out by studying various parameters such as dielectric constant (ε'), electrical modulus (M), tangent loss (tan δ), AC conductivity (σ_{ac}) and dielectric loss (ε″) using an LCR meter. The ternary PANI–ZnO–PPy nanocomposite shows high values for both ε' and σ_{ac} parameters within the given spectrum of frequency (10^3–10^6 Hz) and for the temperature range (30 to 150 °C) than the PANI–PPy nanocomposite. From these results, it confirm that the synthesized ternary material could be used as a key material in the fabrication of optoelectronic devices as well as in energy storage devices.

2 Experimental Procedure

2.1 Materials

Zinc nitrate hexahydrate (Zn $(NO_3)_2 \cdot 6H_2O$), aniline ($C_6H_5NH_2$), pyrrole (C_4H_5N), hydrochloric acid (HCl), ammonium persulphate (APS), ferric chloride ($FeCl_3$) were purchased from Sigma-Aldrich. Acetone (C_3H_6O), ethanol (C_2H_5OH) and sodium hydroxide (NaOH) were purchased from Merck. Deionized water was used as solvent throughout the experiment and all the chemicals and reagents were utilized without further purification.

2.2 Synthesis of ZnO Nanoparticles

Presently, ZnO nanoparticles have been synthesized by using a hydrothermal approach. At first, 4 g of zinc nitrate hexahydrate (Zn $(NO_3)_2$ $6H_2O$) was dissolved in 50 mL of deionized water and magnetically stirred at room temperature for about 30 min. In the meantime, 10 g of sodium hydroxide (NaOH) pellets were dissolved in 50 mL of deionized water and stirred continuously at room temperature for 30 min to yield 5 M of NaOH solution. Then, the prepared 5 M NaOH solution was added dropwise to the previous Zn $(NO_3)_2$ $6H_2O$ solution to undergo the stirring process for a duration of 4 h. Following that, the obtained precipitate was poured in a Teflon lined stainless-steel autoclave and placed in a muffle furnace for 16 h at a temperature of 180 °C. After heating, the product was cooled at room temperature and washed multiple times with deionized water and ethanol to remove other organic analytes. Finally, the resultant precipitate was dried at 100 °C for 12 h in a hot air oven and calcined at 500 °C for 2 h to obtain white coloured ZnO nanoparticles.

2.3 Synthesis of PANI–PPy Nanocomposite

The chemical oxidative polymerization technique was used to synthesize the binary PANI–PPy nanocomposite. At first, 0.5 M aniline and 0.5 M pyrrole were dissolved in 50 mL of deionized water. Addition of 2 g of APS (strong oxidant) and 0.2 M of $FeCl_3$ (weak oxidant) to the above solution initiated the process of polymerization. Continuous stirring of this mixture at room temperature for 12 h duration resulted in the completion of the polymerization reaction. After stirring, the obtained product was filtered and washed with ethanol and deionized water several times to remove the organic trace elements. In order to attain PANI–PPy nanocomposite, the final product was dried in a hot air oven at 60 °C for 12 h.

2.4 Synthesis of PANI–ZnO–PPy Nanocomposite

The in situ chemical oxidative polymerization technique was used to prepare the ternary PANI–ZnO–PPy nanocomposite in the presence of strong oxidizing agents such as ammonium per sulphate (APS) and ferric chloride ($FeCl_3$). Initially, 3 g of synthesized ZnO and 3.5 M of aniline monomer were dispersed in 50 mL of deionized water. To this solution, 0.2 M of APS and 1 M of HCl was added drop by drop and magnetically stirred for 2 h at room temperature. During that time, 3 M of pyrrole monomer and 2 g of $FeCl_3$ were dissolved in 50 mL of deionized water and stirred continuously for an hour. This solution was slowly added to the aniline contained solution and continuously stirred for 12 h. As a result, the obtained product was in deep black color which was filtered 2–3 times with deionized water and later on dried at 60 °C for 12 h. The step by step synthesis procedure of PANI–ZnO–PPy nanocomposite is illustrated in schematic diagram Fig. 1.

2.5 Characterization

The phase formation of unary ZnO and ternary PANI–ZnO–PPy nanocomposite were analyzed through X-ray diffractometer (XRD-GBCMMA) using (Cu-Kα radiation, = 1.5406 Å) as the X-ray source and the XRD patterns were recorded in the 2θ range 10˚-80˚at room temperature. Fourier transform infrared spectroscopy (FTIR) measurements were carried out using Perkin Elmer spectrophotometer in attenuated total reflection (ATR) mode to determine the presence of functional groups in the synthesized ZnO nanoparticles and PANI–ZnO–PPy nanocomposite. The thermal stability of ternary nanocomposite has been evaluated through thermogravimetric analysis (TGA) using Pyris1 TGA (Perkin-Elmer) at a heating rate of 10 °C min^{-1} from 30 to 800 °C in the presence of nitrogen environment. FESEM-EDAX techniques (COXEM-200TM) were performed to investigate the surface topology and elemental composition of the PANI–ZnO–PPy nanocomposite. Using UV–Vis spectroscopy (CARY-5000) in the 200–800 nm wavelength range, the optical activity of unary ZnO nanoparticles and PANI–ZnO–PPy nanocomposite were investigated.
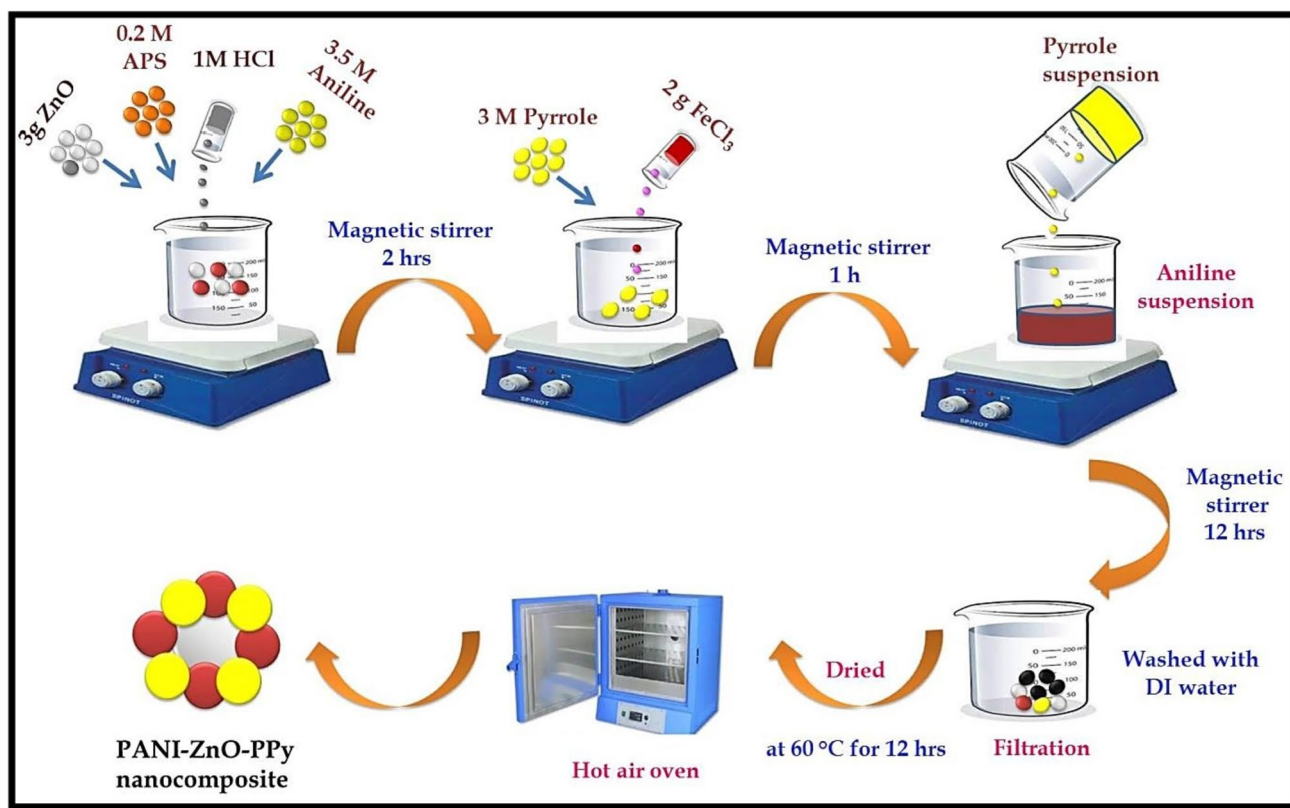
Fig. 1 Preparation of PANI–ZnO–PPy polymer nanocomposite

2.6 Dielectric Measurements

The as-prepared PANI–PPy and PANI–ZnO–PPy nanomaterials were first crushed into a fine powder and then formed into disk-shaped pellets with a diameter of 7 mm and a thickness of 10 mm with the help of hydraulic press under 3 tons cm^{-2}. Next, the dielectric characterization of the pelletized nanomaterials were carried out after coating both the sides of the pellets with silver paste that acted as two parallel plates. After that, the coated nanomaterial pellets were placed in a muffle furnace annealed at 140 °C for two hours before taking the dielectric measurements. The dielectric analyses of both the binary and ternary nanocomposites were recorded by using a programmable automatic LCR bridge (HIOKI: 3532–50). The resultant dielectric data was composed of studies pertaining to parameters such as resistance (R), capacitance (C), delay angle (θ) and impedance (Z) for a varying frequency and temperature range. Using the above acquired data, the various dielectric properties of the nanocomposites were evaluated.

3 Results and Discussion

3.1 XRPD Analysis

X-ray diffraction is a very effective technique to determine the phase, structure and crystallite size of materials in the micro and nano scale. In Fig. 2a–d, the XRD spectra of unary PANI, PPy, ZnO and ternary PANI–ZnO–PPy nanomaterials are displayed. The XRD spectrum of the as-synthesized PANI nanoparticles (Fig. 2a) exhibit the broad diffraction peaks at 20.1° and 25.8° corresponding to (020) and (200) planes, respectively. The XRD spectrum of PPy nanoparticles (Fig. 2b) shows the broad reflection peaks at 15.1° and 25.3° corresponding to (011) and (200) planes, respectively. The low intensity broad peaks confirm the amorphous nature of PANI and PPy polymers [26, 27].

The obtained XRD spectrum of ZnO affirms the crystalline nature which is depicted in Fig. 2c. The crystallite peaks at 2θ = 31.7°, 34.3°, 36.2°, 47.4° 56.4° 62.7°, 66.3°,
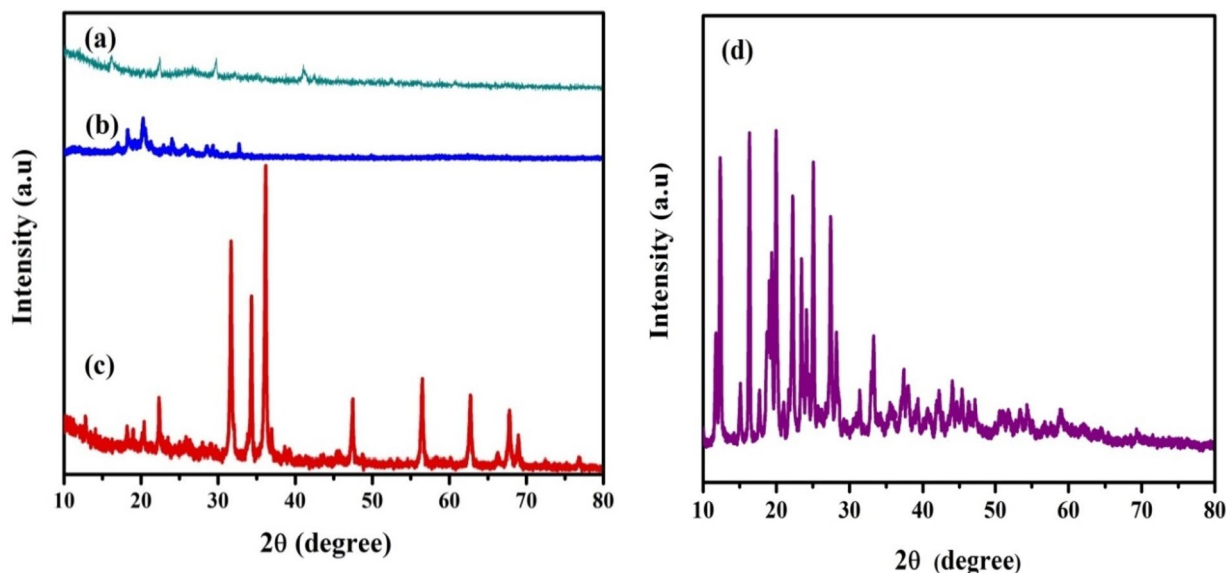
Fig. 2 Diffraction patterns of **a–c** unary PANI, PPy, ZnO and **d** ternary PANI–ZnO–PPy nanomaterials

68.2˚and 69.0˚are corresponding to various miller indices including, (100), (002), (101), (102), (110), (103), (200), (212) and (201) of the crystalline planes. All these diffraction peaks indicate the hexagonal-close-packed wurtzite crystal structure of ZnO which are in well accordance with the formerly reported research work (JCPDS No. 00–036-1451) [28]. No extra peaks in the XRD pattern, confirms the purity of the as-prepared ZnO nanoparticles.

The diffraction curve of PANI–ZnO–PPy polymer nanocomposite is illustrated in Fig. 2d. The low intensity peaks detected at 15.4˚, 20.3˚, 25.3˚ and 27.1˚ are assigned to (0 1 1), (0 2 0), (2 0 0) and (1 2 1) planes in PANI–ZnO–PPy nanocomposite. These peaks confirm the presence of PANI and PPy polymers in PANI–ZnO–PPy, caused by quinoid and benzenoid ring repetition in polymeric chains. Also, the characteristic diffraction peaks detected at 28.3˚, 31.3˚, 33.4˚, 36.4˚, 39.3˚, 42.2˚, 43.9˚, 45.3˚, 46.1˚, 47.8˚, 54.4˚, 59.1˚ and 69.3˚ in the XRD pattern of PANI–ZnO–PPy strongly shows the existence of ZnO nanoparticles in the ternary polymer nanocomposite. However, the detected ZnO peaks in the ternary nanocomposite are found to have a slight shift from their corresponding peak position, which is primarily owing to the interaction between polymer PANI–PPy matrix and inorganic ZnO. The deviation of the standard ZnO peaks in the XRD pattern of PANI–ZnO–PPy, which also lack sharp intensity, is owing to the influence of amorphous polymers with crystalline phase of ZnO. Hence, it is clearly seen from the XRD pattern that the amorphous nature of polymeric PANI–PPy matrix has been masked by the crystallinity of ZnO nanoparticles and has resulted in the semi-crystalline phase of PANI–ZnO–PPy. Further, the crystallite size 'D' of unary

and ternary materials was evaluated using the Scherer formula [29], as given in Eq. 1.

$$D = \frac{k\lambda}{\beta Cos\theta} \qquad (1)$$

where, k-geometry factor (k = 0.94), λ-wavelength of the X-ray (Cu kα, 1.54 Å), β-full width at half maximum (FWHM), θ-difraction angle. The calculated crystallite size of PANI–ZnO–PPy nanocomposite is found to be lower 17 nm while compared to the ZnO nanoparticles 26 nm.

3.2 FESEM/EDAX Analysis

The FESEM images of PANI–ZnO–PPy nanocomposite as seen in Fig. 3a–d displays the micrograph and nanograph morphological features at different magnifications. A homogenous pattern of mostly spherical shaped particles can be seen for all magnifications, which have agglomerated to form several clusters. In particular, the topography of the particles viewed at 500 nm clearly shows that their spherical symmetry is lost due to the successful polymerization of polymer PANI–PPy matrix around ZnO nanoparticles. At 5 μm and 3 μm, the images show particle clusters with well-developed granular regions. The morphological image at 500 nm magnification not only shows uniform dispersion of particles with many pores but also clearly reveals intergranular regions apart from the individual grains. Thus, FESEM study of PANI–ZnO–PPy exhibits large number of agglomerations due to the increase in interactions between all the unary nanoparticles. The more number of agglomerations gives the appearance of dense granular morphology
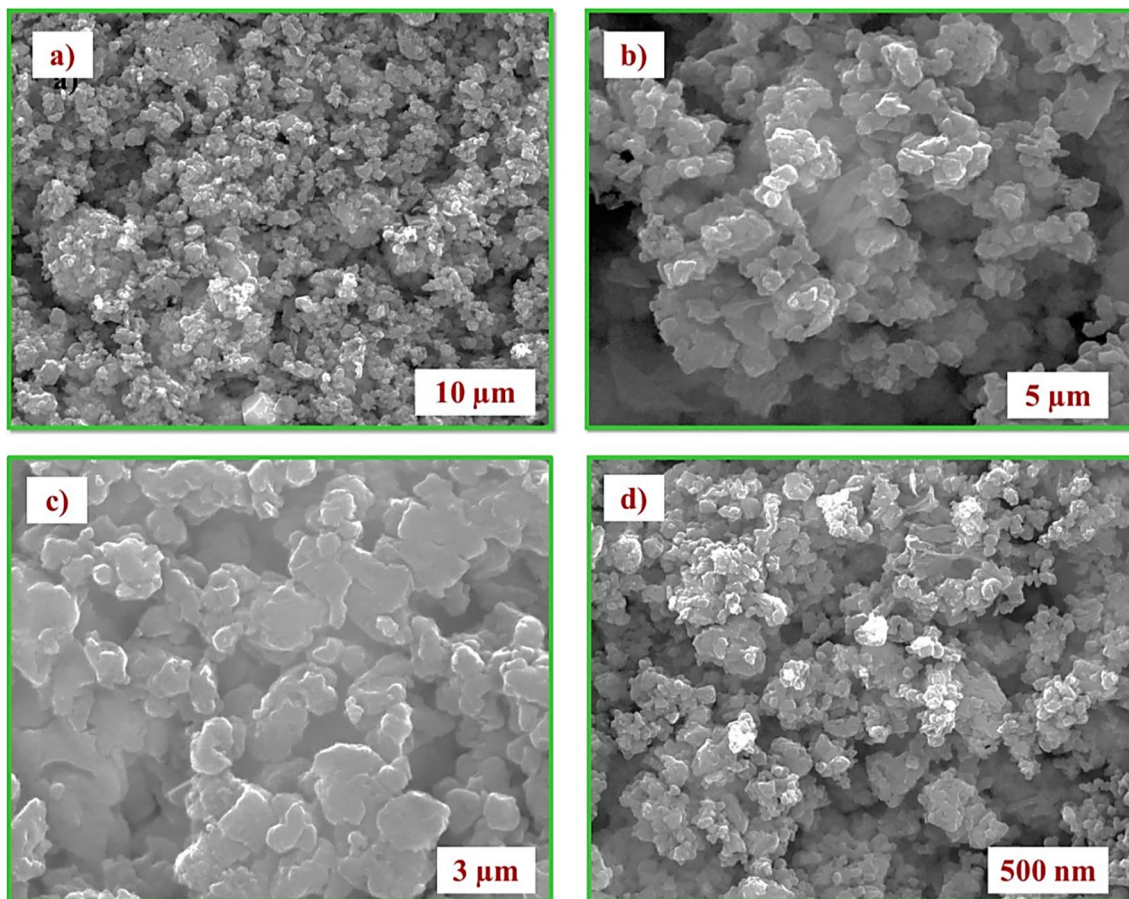
Fig. 3 **a–d** illustrates the FESEM of PANI–ZnO–PPy nanocomposite

of porous particles and such synthesized materials are suitable for various applications like gas sensing, catalytic, energy storage and electronic devices. Further, the identification of various elements including C, N, O and Zn in the EDAX spectrum of PANI–ZnO–PPy (Fig. 4a) confirms the presence of conducting polymers and metal-oxide in the PANI–ZnO–PPy nanocomposite. The elemental distribution within the ternary material is studied through their respective mapping images as illustrated in Fig. 4b–f and the weight percentages of C, N, O and Zn elements are found to be 54.83%, 12.96%, 17.73%, and 14.48%, respectively. This reveals that the synthesized ternary nanocomposite is dominated by the polymeric materials in comparison with inorganic ZnO nanoparticles due to the presence of large quantity of carbon (54.83%) in it.

3.3 TGA Analysis

The primary intention of this study is to evaluate the material's suitability for optoelectronic devices in an environment where a temperature variation is anticipated. In this context, the thermal behavior of PANI–ZnO–PPy nanocomposite was

studied to ensure its operational limit when used as an optoelectronic device in a high temperature region. The TGA technique was carried out from the ambient temperature of 30 °C to a high temperature of 800 °C in order to understand the thermal characteristics and stability of the synthesized PANI, PPy, ZnO nanoparticles and ternary polymer PANI–ZnO–PPy nanocomposite under inert atmospheric conditions.

In general, thermal stability of nanocomposites is influenced by number of aspects such as nano filler concentration, morphological structure and interfacial interactions of the individual components present in the nanocomposite [30]. The TGA curves of PANI and PPy (Fig. 5a) indicate their low thermal stability. As they come under the category of organic conducting polymers, nearly 70 weight % of PANI and 60 weight % of PPy has been degraded at a high temperature of 800 °C. Only 30 weight % of PANI and 40 weight % of PPy remains undegraded and is obtained as a final residue. The TGA curve of ZnO nanoparticles (Fig. 5a) indicates its high thermal stability. Metal-oxide ZnO, being inorganic in nature results in a very high char residue (92%) at a high temperature of 800 °C. This means that only 8% of
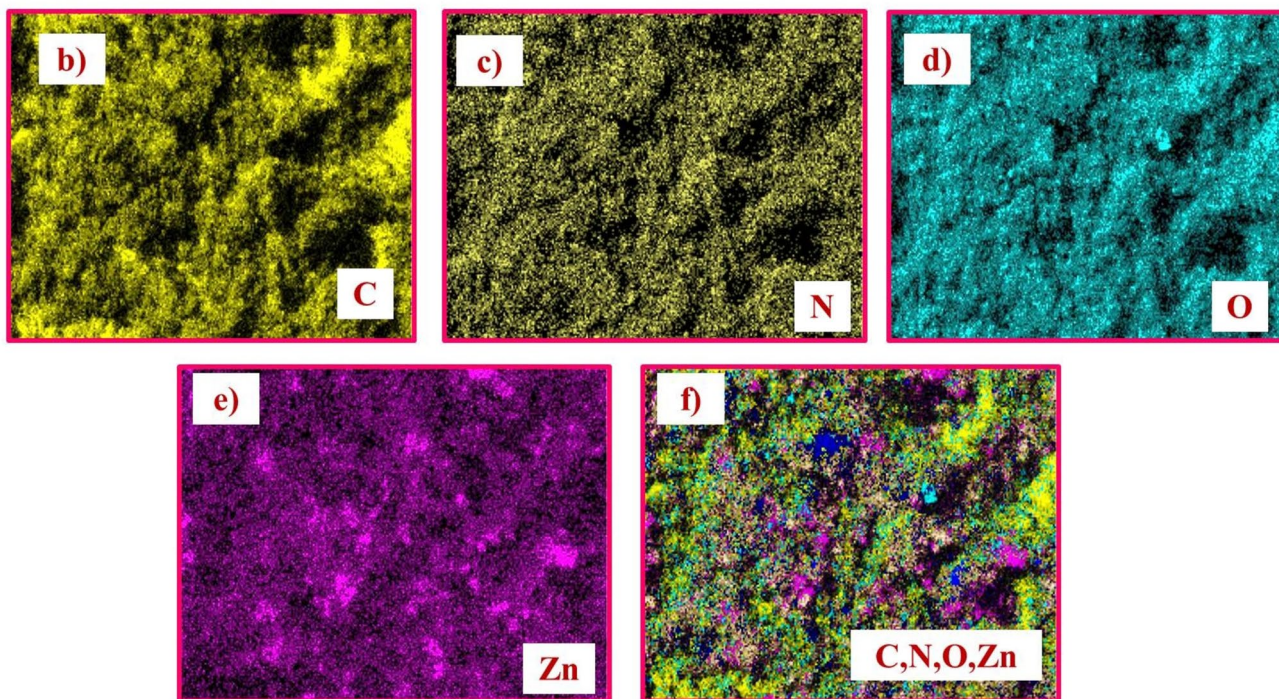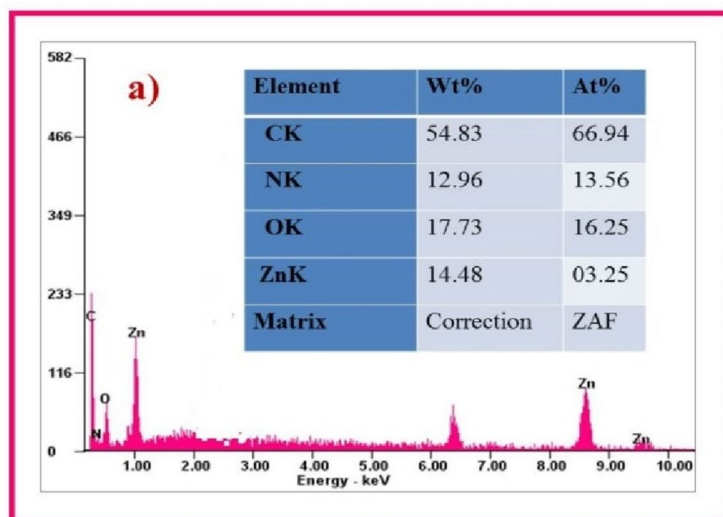
Fig. 4 **a** EDAX and **b**–**f** Elemental mapping of ternary PANI–ZnO–PPy nanocomposite

ZnO has been decomposed and the remaining 92% remains undegraded. The initial decomposition of 8% is due to the loss of adsorbed water molecules from ZnO. As the temperature is increased, the TGA curve of ZnO becomes more or less parallel to the temperature axis which means the metal-oxide shows no water loss resulting in a high char yield.

Figure 5b shows the three-step decomposition of ternary PANI–ZnO–PPy nanocomposite. Initially, a small amount of weight loss (14%) occured in 45–110 °C, which is due to the surface-level evaporation of hydroxyl groups present in the ternary nanocomposite [31]. A second stage of weight loss (29%) takes place in the temperature range of 110–250 °C, implying the elimination of oligomers and dopant molecules from the surface of the polymer chains. The ternary material loses 51% of its weight during the final stage of degradation, which is detected in
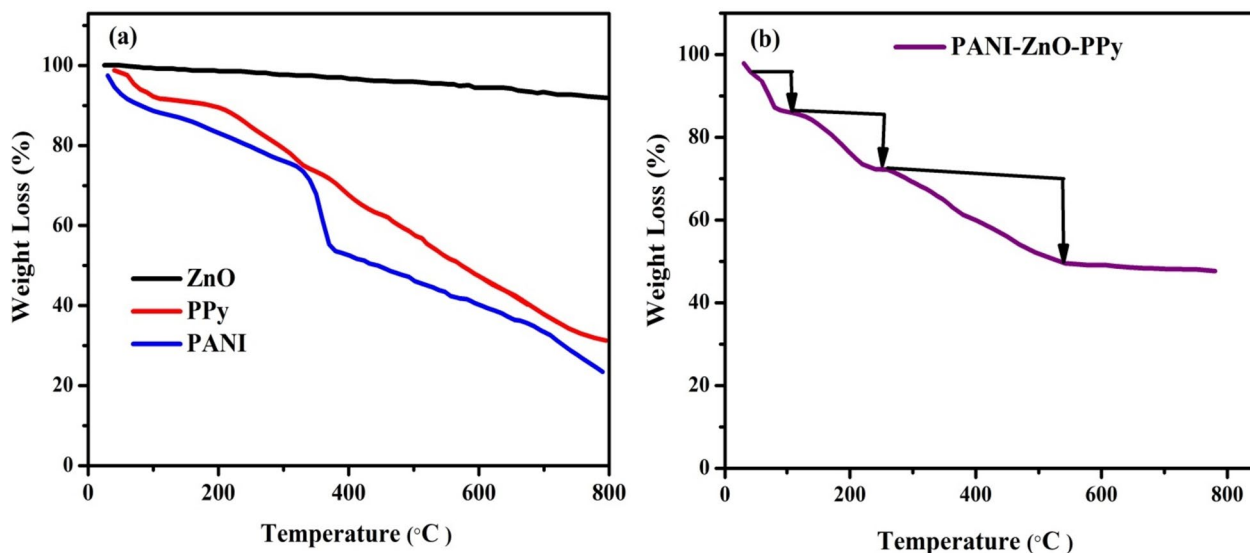
Fig. 5 Displays the TGA curves of **a** unary PANI, PPy and ZnO nanoparticles and **b** ternary PANI–ZnO–PPy nanocomposite

250 to 540 °C temperature range. The final degradation step is ascribed to the complete disruption of polymer (PANI–PPy) chains present in PANI–ZnO–PPy. In general, the complete removal of the polymeric backbone structure from any composite takes place in this high temperature range, which is also confirmed in the present material [32]. Due to the existence of aromatic rings and inorganic components, 49% of ternary PANI–ZnO–PPy nanocomposite remains as a residue material at 800 °C. The residue at

such a high temperature cannot be due to organic constituents but is mainly due to the presence of inorganic ZnO component in the ternary material. The distribution of ZnO nanoparticles in a homogenous manner within the polymeric (PANI–PPy) matrix, as affirmed from FESEM images (Fig. 3) has not only resulted in a high char yield but has also promoted and improved the thermal stability of PANI–ZnO–PPy. Thus, the structure, degree of crystallinity and the molecular weight of the organic–inorganic components present has played a vital role in determining the thermal properties of PANI–ZnO–PPy [33].
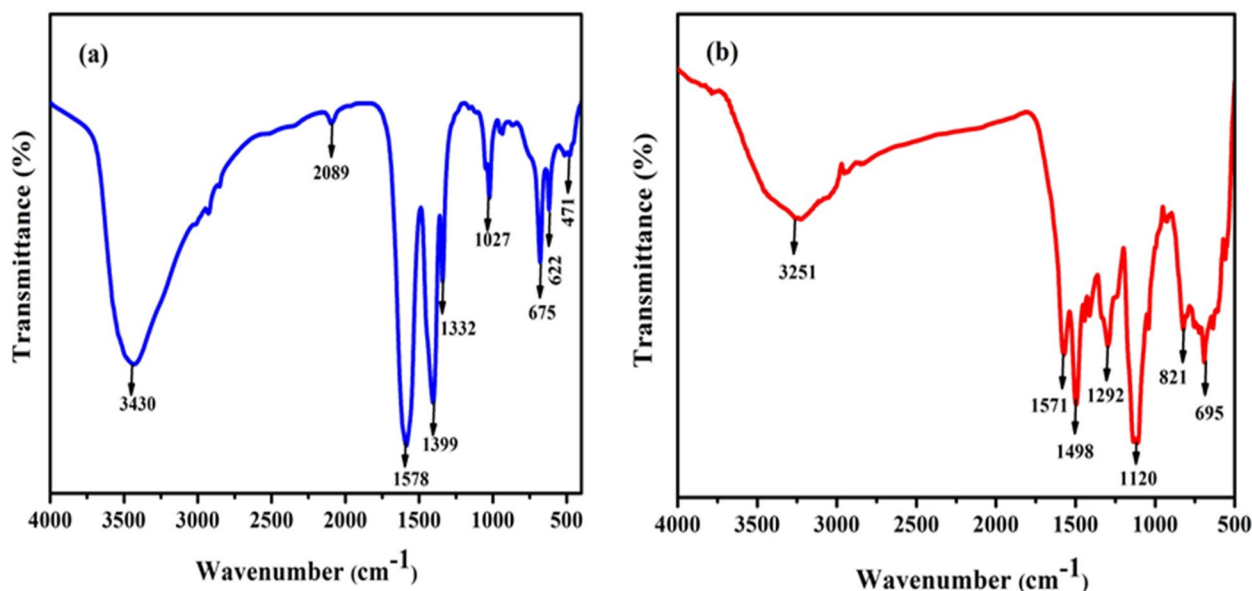
Fig. 6 FTIR spectra of the as-prepared: **a** ZnO nanoparticles and **b** PANI–ZnO–PPy nanocomposite

3.4 Fourier Transform Infrared Spectroscopy (FTIR)

FTIR Spectroscopy is well known analytical technique that can give the information about the functional groups, bond angle and bond length of the as-synthesized ZnO and PANI–ZnO–PPy nanomaterials were determined in the range of 400 to 4000 cm^{-1} as depicted in Fig. 6a, b. Figure 6a shows that the broad absorption band around 3430 cm^{-1}, which is related to the O–H groups stretching vibrations in ZnO nanoparticles. The occurrence of this band is due to surface-level atmospheric interaction of the inorganic nanoparticles [34]. The small absorption peak at 2089 cm^{-1} can be ascribed to C–N stretching vibrations. Sharp and medium intensity peaks detected at 1578 cm^{-1} and 1027 cm^{-1} are due to C–O stretching vibrations and the additional peaks detected at 1399 cm^{-1} and 1332 cm^{-1} are assigned to C–H stretching vibrations. These molecular vibrational frequencies of ZnO nanoparticles originate due to the interaction of the structural molecules with environmental elements [35]. Strong absorption peaks exhibit at 675 cm^{-1}, 622 cm^{-1} and 471 cm^{-1} are assigned to Zn–O vibration mode, which confirms the formation of metal oxide nanoparticles. All the peaks presented in ZnO nanoparticles are found to match well with previous literature [36]. As seen in Fig. 6b, the synthesized PANI–ZnO–PPy nanocomposite displays the distinct peaks of the PANI and PPy polymers and also shows ZnO nanoparticles peaks with a little change in vibrational frequencies. The broad band identified at 3251 cm^{-1} is related to the adsorption of water (H_2O) molecule on the external surface of the ternary material. The absorption peak found at 695 cm^{-1} is attributed to the Zn–O stretching vibration, which affirms the formation of ZnO

nanoparticles in PANI–ZnO–PPy nanocomposite. Further, a frequency shift of the distinctive peaks arises at 1571 cm^{-1}, 1498 cm^{-1}, 1292 cm^{-1}, 1120 cm^{-1} and 821 cm^{-1} in the spectrum of PANI–ZnO–PPy due to the effective interaction of all the individual nanoparticles in the ternary material.

3.5 UV–Vis spectroscopy Analysis

The optical activity of nanoscale materials were investigated using the UV–Visible spectroscopic technique. As shown in Fig. 7a, b, the absorbance of PANI–ZnO–PPy and ZnO nanomaterials was studied as a function of wavelength in the range of 200–800 nm. A characteristic peak at 398 nm in the absorption spectrum of the ZnO nanoparticles (Fig. 7a) is attributed to the electronic transitions (Zn_{3d}-O_{2p} transitions) from the valence to the conduction band in the hexagonal phase of inorganic ZnO [37]. The UV–Visible spectrum of PANI–ZnO–PPy nanocomposite (Fig. 7b) displays four distinctive absorption peaks at 233, 280, 396 and 441 nm, respectively. The absorption peaks detected at 233 and 280 nm are associated with the π–π* electron transitions in benzenoid units of the polymers [38]. The peak detected at 396 nm confirms the existence of ZnO nanoparticles in the ternary nanocomposite and the peak observed at 441 nm is related to polaron-π* transition in the binary PANI–PPy polymers [39].

3.5.1 Optical Band Gap Energy

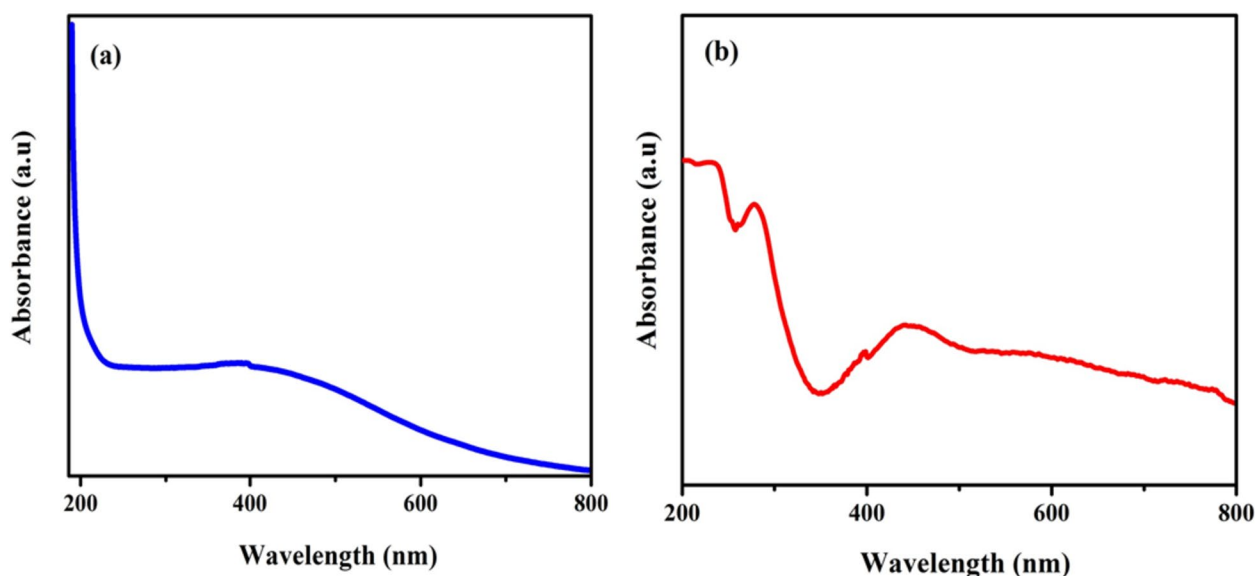The optical band gap energy of ZnO nanoparticles and PANI–ZnO–PPy nanocomposite was evaluated from

Fig. 7 UV–Visible spectra of **a** ZnO and **b** PANI–ZnO–PPy nanocomposite

UV–Vis absorption data using the Tauc's relation [40] as expressed in Eq. 2.

$$(\alpha h\nu)^{1/n} = A\big(h\nu - E_g\big) \tag{2}$$

where α-absorption coefficient, h-Planck's constant, ν-frequency of light, A-absorption constant and E_g-band gap of the material. The value of 'n' is 1/2 for a direct mode of transition and 2 for an indirect mode of transition. A band-to-band optical transition completely depends on the band structure of the material and the transition probability differs significantly between a direct band gap and indirect band gap material. Generally, there is no change in momentum during the electronic transitions in a direct band gap material and the difference in energy during the downward transition rate is given out as photons without the participation of phonons. On the other hand, de-excitation of electrons during the downward transitions involves exchange of energy and momentum to the lattice in an indirect band gap material. Subsequently, the lattice vibration results in the emission of energy in the form of phonon. For this reason, direct band gap materials are widely opted for use in optoelectronic devices.

To evaluate the band gap of the unary and ternary nanomaterials, a plot of absorption coefficient $(\alpha h\upsilon)^2$ versus photon energy $(h\upsilon)$ is depicted in Fig. 8a, b. The extrapolated straight line at the absorption edge is made to intercept the photon energy $(h\upsilon)$ along the x-axis. The intercept directly gives the band gap value of the as prepared nanomaterials. The calculated bandgap values for ZnO nanoparticles and PANI–ZnO–PPy nanocomposite are found to be 3.34 eV and 2.92 eV, respectively and the value of ZnO

(3.34 eV) is in good accord with the previously reported research work [41]. The obtained band gap value of ternary PANI–ZnO–PPy nanocomposite is lower in comparison with ZnO nanoparticles. This has happened owing to the interactions of the individual components that have played their part in tailoring the energy gap of ternary PANI–ZnO–PPy. The complimentary interaction of PANI, ZnO and PPy within the ternary nanocomposite must have incremented several factors such as the defects states, vacancies/interstitials not only in the regular structure but also in the grain boundary positions of PANI–ZnO–PPy. All these factors must have initiated the occurence of new localized energy states in the ternary PANI–ZnO–PPy, leading to the reduction of bandgap. Hence, the lowest band gap reveals that the synthesized PANI–ZnO–PPy nanocomposite is a potential candidate for optoelectronic devices.

3.6 Dielectric Properties

After exploring the dielectric characteristics of binary PANI–PPy and ternary PANI–ZnO–PPy nanocomposite as a function of frequency (1 kHz to 1 MHz) and temperature (30 to 150 °C), the following parameters were evaluated.

3.6.1 Dielectric Constant (ε')

The dielectric constant (ε') is a crucial parameter which shows how well materials can store electrical energy in the presence of an applied electric field. The following equation is used to determine the dielectric constant for PANI–PPy and PANI–ZnO–PPy materials at various temperatures [42].
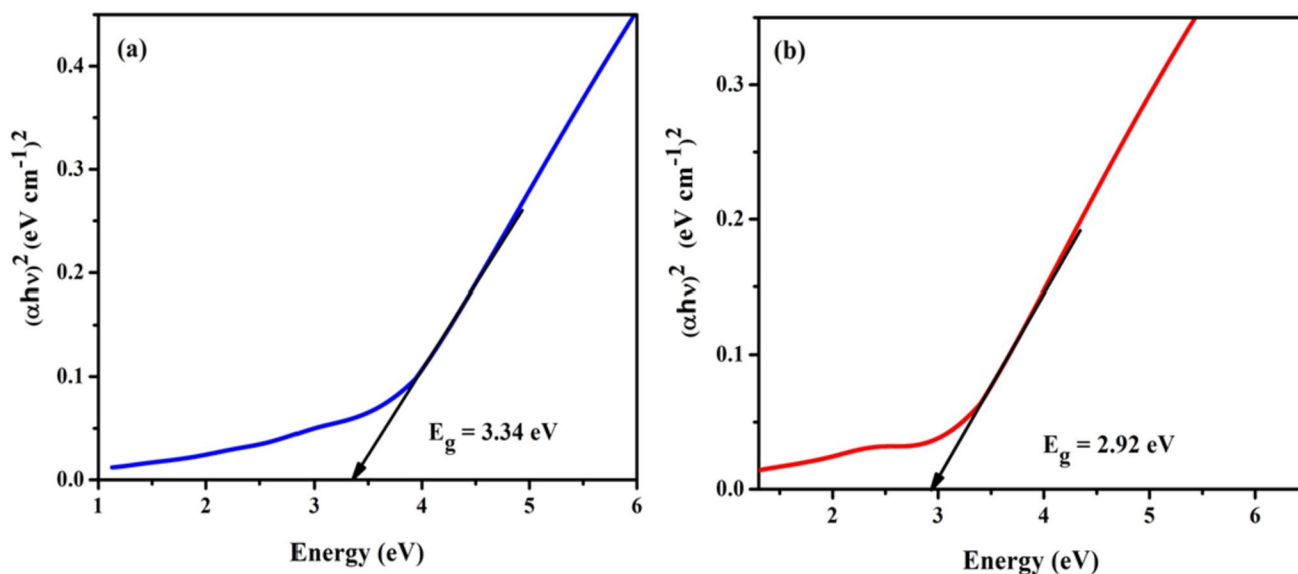
Fig. 8 Band gap spectra of **a** ZnO nanoparticles and **b** PANI–ZnO–PPy nanocomposite
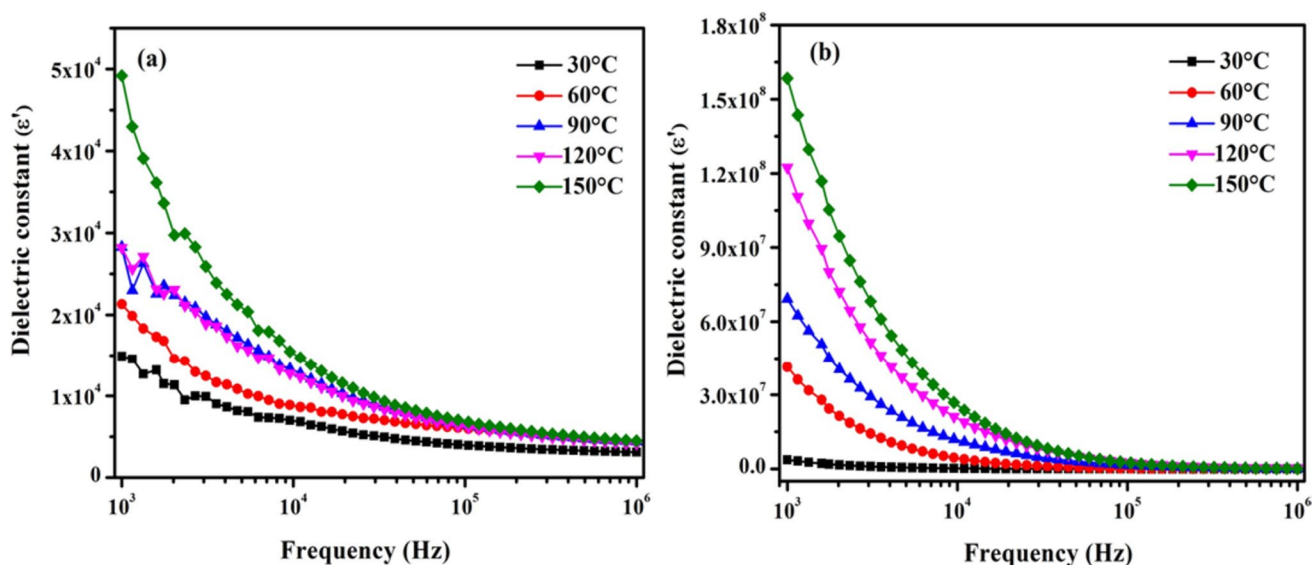
Fig. 9 Dielectric constant curves for **a** PANI–PPy and **b** PANI–ZnO–PPy at different temperatures

$$\varepsilon' = \frac{\text{Cd}}{\varepsilon_0 A} \tag{3}$$

where, C-capacitance in Farad, d-thickness of the pellet (mm), ε_0-permittivity of free space (8.85×10^{-12} N m^2) and A-cross-sectional area (m^2) of the as prepared binary and ternary nanocomposites.

Figure 9a, b illustrates the dielectric constant (ε') curves of as-synthesized binary and ternary nanomaterials in the frequency range of 1 kHz to 1 MHz for various temperatures ranging from ambient temperature of 30 °C to a higher temperature of 150 °C. The binary and ternary materials exhibited a frequency-dependent phenomenon, in which the ε' value decreases rapidly with a frequency rise, which follows the general trend [43]. The ε' values of both the nanocomposites is high in the low frequency region as there was sufficient time for the alignment of molecular dipoles with the applied field owing to the Maxwell Wagner polarization effect [44], and this trend was seen in the entire temperature range (30–150 °C). At the same time, the ε' decreases at higher frequency region for the temperature range (30 °C to 150 °C) because of the incapability of the dipole molecules to align with the applied field in the short duration of time. It can also be inferred from Fig. 9a, b that the ε' values for both the nanocomposites tend to increase with increasing temperature. The dielectric constant (ε') values for binary and ternary nanocomposites are found to be high at 150 °C for a low frequency of 1004 Hz. It is because the dipole molecules have received sufficient thermal energy to respond/align themselves quickly in the applied field leading to the increase of interfacial polarization. Meanwhile, the dielectric constant (ε') values for both the nanocomposites are found

to be minimum at a low temperature of 30 °C at a frequency of 1002 Hz. This is due to the lack of sufficient thermal energy for dipole molecules to align with the applied field. At 150 °C, the dielectric constant value of PANI–PPy and PANI–ZnO–PPy nanocomposites are found to be 4.33×10^4 and 1.453×10^8 at 1000 Hz, respectively. Thus, the dielectric studies show that the ternary PANI–ZnO–PPy nanocomposite has a relatively higher dielectric constant value than the binary PANI–PPy nanocomposite, which is owing to the active inclusion of ZnO nanoparticles into the binary PANI–PPy network. This synergistic interaction has led to the increase of defects like dislocations and oxygen vacancies in the ternary material and has paved the way for the increment in the dielectric constant value. This result also suggests that all the possible defects have not only increased the polarization mechanism within the granular structure but has also effectively increased the polarization at the interface between two grain boundaries.

3.6.2 Dielectric Loss (ε'')

In any dielectric material, the dielectric loss parameter (ε'') accounts to the amount of energy loss, which happens due to the passage of E.M waves through it. The dielectric loss is dependent on the nature of the dielectric and the applied frequency. Using the following relation given in Eq. 4, the dielectric loss parameter was calculated [45].

$$(\varepsilon'') = (\varepsilon') \tan\delta \tag{4}$$

where, ε'—dielectric constant and tan δ—tangent loss. The frequency-dependent behavior of dielectric loss (ε'') and
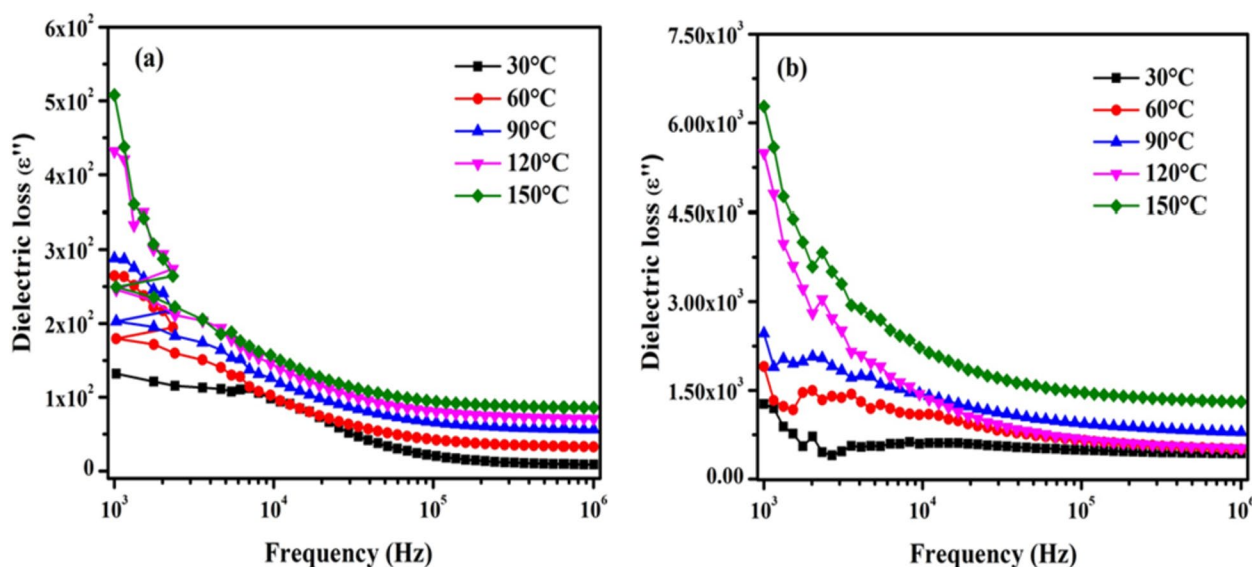
Fig. 10 Dielectric loss curves for **a** PANI–PPy **b** PANI–ZnO–PPy nanocomposite at different temperatures

its relevant curves shows the similar trend like dielectric constant for both the nanocomposites. The dielectric loss (ε'') as a function of frequency and temperature for both PANI–PPy and PANI–ZnO–PPy nanocomposites is shown in Fig. 10a, b. Typically, the dielectric loss is mainly attributed to the relaxation of molecular dipoles in the synthesized nanocomposites [46]. From the plots, the dielectric loss value for as-prepared nanocomposites increases at low frequency range, decreases at mid frequency and does not show appreciable variation at higher frequency range. At low frequency region, ε'' increases for both binary and ternary nanocomposites from the room temperature of 30 °C to a high temperature of 150 °C due to the increase in the density of charge carriers at the grain boundary regions [47]. Whereas, in the higher frequency region, the value of ε'' decreases due to the reduction of the charge carrier density reduces at the grain boundary locations. Figure 10a, b also indicates the increase in ε'' values for PANI–PPy and PANI–ZnO–PPy with increasing temperature. The dielectric loss value of PANI–PPy at 10^3 Hz is found to be 5.13×10^2 at 150 °C. But in the ternary PANI–ZnO–PPy nanocomposite, dielectric loss value is found to be relatively higher, i.e., 6.33×10^3 at 150 °C. The high dielectric loss exhibited by the ternary nanocomposite in comparison with binary nanocomposite is due to the accumulation of more number of charge carriers in the interface between the polymeric matrix and metal oxide nanofiller, which also plays a vital role in improving the charge storage capacity of synthesized ternary nanocomposite.

Therefore, the ternary PANI–ZnO–PPy nanocomposite has the potential to be used in multiple applications, and specifically as energy storing materials in capacitors, cooling agent in transformers and performance enhancer in semiconductor devices.

3.6.3 Tangent Loss (Tan δ)

Generally, the dielectric tangent loss occurring in a material is largely influenced by crucial physical processes, namely, dielectric resonance, dielectric relaxation, electrical conduction and loss from non-linear processes [48]. The tangent loss is an essential parameter to explore the dissipation of electrical energy in the dielectric and hence depends on both frequency and temperature. The following equation is used to evaluate the materials dissipation factor [49].

$$tan\delta = \frac{\varepsilon''}{\varepsilon'} \tag{5}$$

where, ε''- dielectric loss and ε'- dielectric constant.

Figure 11a, b displays the tangent loss curves for PANI–PPy and PANI–ZnO–PPy nanocomposites in a temperature range of 30 °C to 150 °C. As shown in Fig. 11a, b, the loss factors of both the nanocomposites decreases with increasing frequency for a fixed temperature. Both the nanocomposites display the high dissipation factor at low frequency region which may arise because of the conduction losses, resistivity of the grain boundaries and other defects. But in the higher frequency regime, the tangent loss decreases for the two nanocomposites due to the small magnitude of charge carriers hopping [50]. The tangent loss value for the synthesized nanocomposites is maximum at a high temperature of 150 °C. The tangent loss values for binary and ternary materials are found to be 6.2886 and
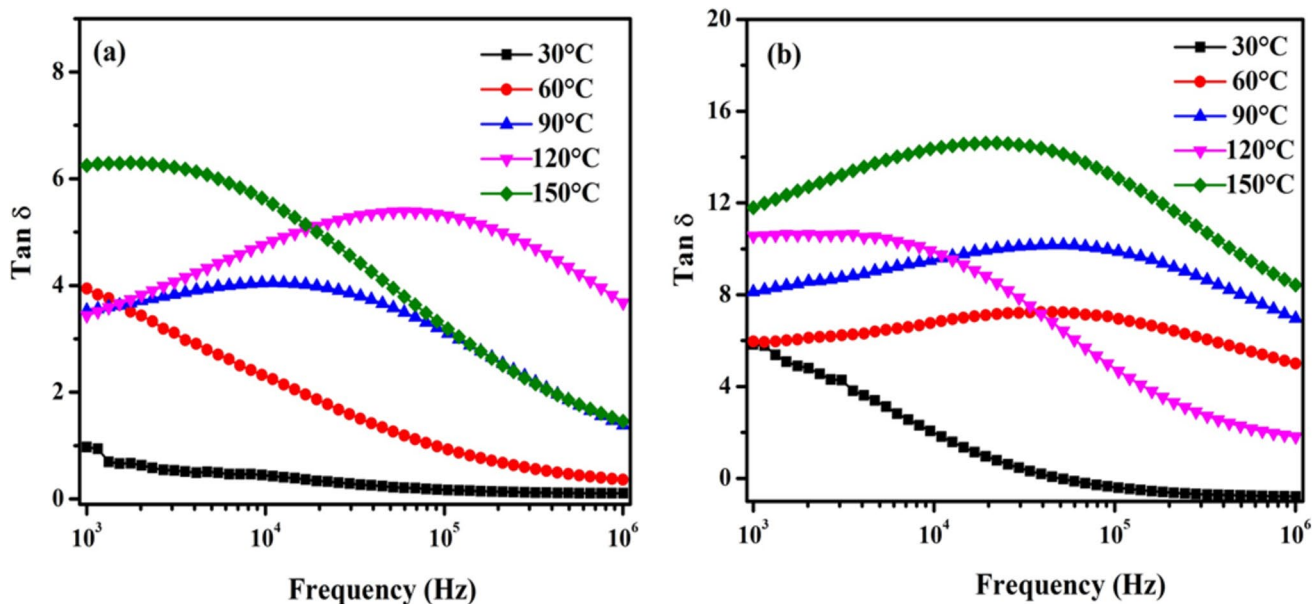
Fig. 11 Tangent loss curves for **a** PANI–PPy, **b** PANI–ZnO–PPy nanocomposite at different temperatures

12.1234, respectively, at 150 °C for 1002 Hz. The tangent loss of ternary PANI–ZnO–PPy is high in comparison with binary PANI–PPy because of the existence of multi-components in the ternary material. In general, the relaxation peaks arise when the charge carriers frequency and the applied electric field frequency are in phase. The loss curves show that the relaxation phenomenon for both binary and ternary materials does not follow a particular trend or is unique for a specific temperature within the specified frequency region. It is because of the interactions between temperature, frequency and moisture content that affect the loss tangent value. Generally, the relationship between loss tangent of a material and the three parameters is quite complex. As frequency increases from 10^3 to 10^6 Hz, the loss tangent values of the nanocomposites show both increasing and decreasing pattern (goes through maximum and minimum values) depending on the temperature and moisture content of the material. To be more precise, the frequency at which the loss tangent becomes maximum/minimum increases with increase in temperature or moisture content. Also, with increasing moisture content, the loss tangent of PANI–PPy and PANI–ZnO–PPy can attain a maximum or minimum value for specific combinations of frequency and temperature. This suggests that the exact relaxation behavior of the nanomaterials could be predicted for various temperatures if the frequency spectrum is enhanced further.

3.6.4 AC conductivity

Using the following equation, the AC conductivity of the binary PANI–PPy and ternary PANI–ZnO–PPy nanocomposites was calculated [51].

$$\sigma = \frac{d}{A} \times \frac{1}{R} \tag{6}$$

where, d-thickness of the pellet (mm), A-cross-section area (cm^2) and R-bulk resistance of the materials (Ω). Figure 12a, b demonstrates the AC conductivity curves of PANI–PPy and PANI–ZnO–PPy nanocomposites within the specified frequency and temperature range. As seen in Fig. 12a, b, the AC conductivity of the nanocomposites does not show significant variation in the low frequency region as the curves are more or less parallel to the frequency axis. Whereas in the higher frequency region, the AC curves show significant variation as seen from their steep increase. The conductivity values of binary and ternary nanocomposites are low in the low frequency region due to the low magnitude of ionic migration within the grains and across the grain boundaries. But in the higher frequency region, both the nanocomposites exhibit high conductivity value, which can be attributed to the large number of migration of ions. Both the binary and ternary nanocomposites show the frequency-dependent behavior of AC conductivity, and exhibits the Maxwell–Wagner model [52]. A similar trend is observed when the temperature is increased gradually from 30 °C to 150 °C. It is seen that the conductivity of the binary and ternary nanomaterials increases with temperature as the polarons gained enough energy to jump over the barrier.
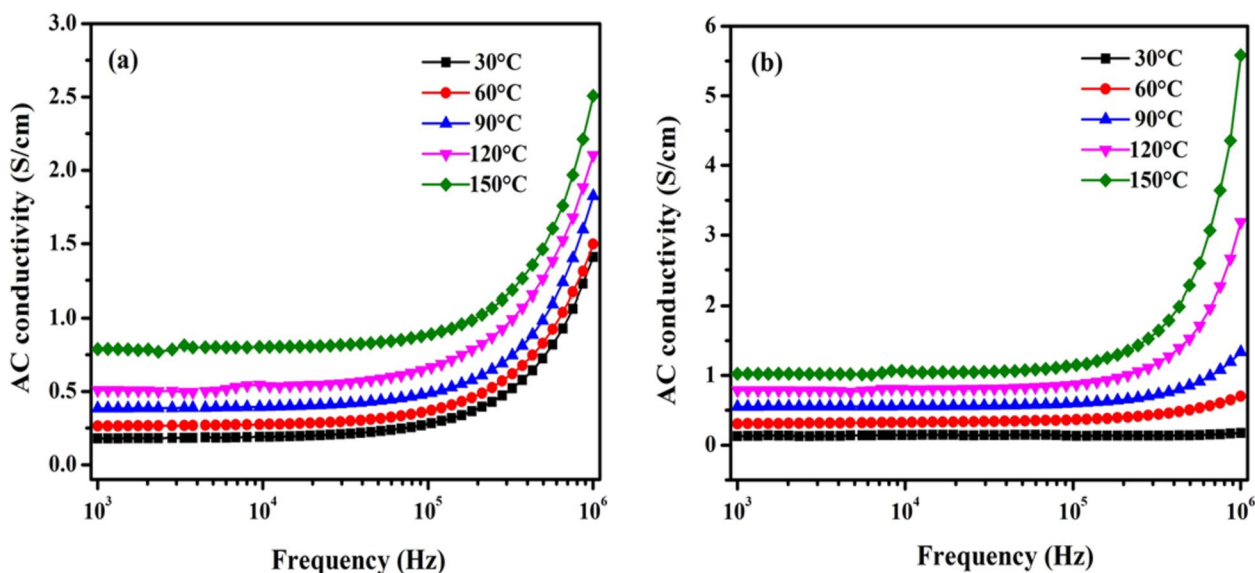
Fig. 12 AC conductivity curves for **a** PANI–PPy and **b** PANI–ZnO–PPy nanocomposite at different temperatures

Moreover, the possibility of inclusion of different types of defects, imperfections and dislocations in the material is high at a higher temperature range leading to the significant enhancement of the mobility of ions. At 150 °C, the AC conductivity values of binary and ternary nanocomposites are found to be 2.5255 S cm^{-1} and 5.5767 Scm^{-1}, respectively, which is higher than that of binary nanocomposite. The PANI–ZnO–PPy nanocomposite exhibits the significant improvement in the conductivity which is owing to the superior interfacial interaction between the unary nanoparticles. The complementary effect of PANI, ZnO and PPy components towards each other has resulted in the creation of large cross-link network and has facilitated the charge transfer across various amorphous and crystalline components in the ternary material. As a result, it can be confirmed that the synthesized ternary material is most suitable to be fabricated as a device for multifunctional electronic device applications.

3.6.5 Electrical Modulus Measurements

Electrical modulus parameter comprises of both real and imaginary components and hence is complex in nature. In fact, Electric modulus (M*) denotes the inverse of complex permittivity and is mainly used to study the charge transport mechanism and dielectric polarization behavior in materials [53]. The following expression is used to determine the complex electric modulus of binary and ternary dielectric materials [54].

$$M^* = M' + jM'' \tag{7}$$

where, M′-real component of electric modulus and M″-imaginary component of electric modulus. Again, M′ and M″ can be determined by using the following equations [55].

$$M' = \frac{\varepsilon'}{\varepsilon'^2 + \varepsilon''^2} \tag{8}$$

$$M'' = \frac{\varepsilon''}{\varepsilon'^2 + \varepsilon''^2} \tag{9}$$

Figure 13a, b shows the real electric modulus (M′) of the binary and ternary nanocomposites as-prepared as a function of frequency (1 kHz to 1 MHz) and temperature (30–150 °C). The real electric modulus of PANI–PPy and PANI–ZnO–PPy nanocomposites increases with increasing frequency and temperature as seen from Fig. 13a, b. In the low frequency region, real electric modulus of both the nanocomposites has a low value due to the absence of significant polarization phenomenon. In the high frequency range, the M′ value gradually rises which indicates the increase in the conduction mechanism within the material due to the quick migration of charge carriers. At a high temperature of 150 °C, the maximum value of M′ for binary and ternary nanocomposites are found to be 3.2307×10^{-4} and 1.0703×10^{-4} at 10^6 Hz, respectively. The values indicate the exhibition of low M′ by the ternary PANI–ZnO–PPy material in comparison with binary PANI–PPy material. This behavior of the ternary nanocomposite is explicitly attributed to the integration of inorganic metal oxide with
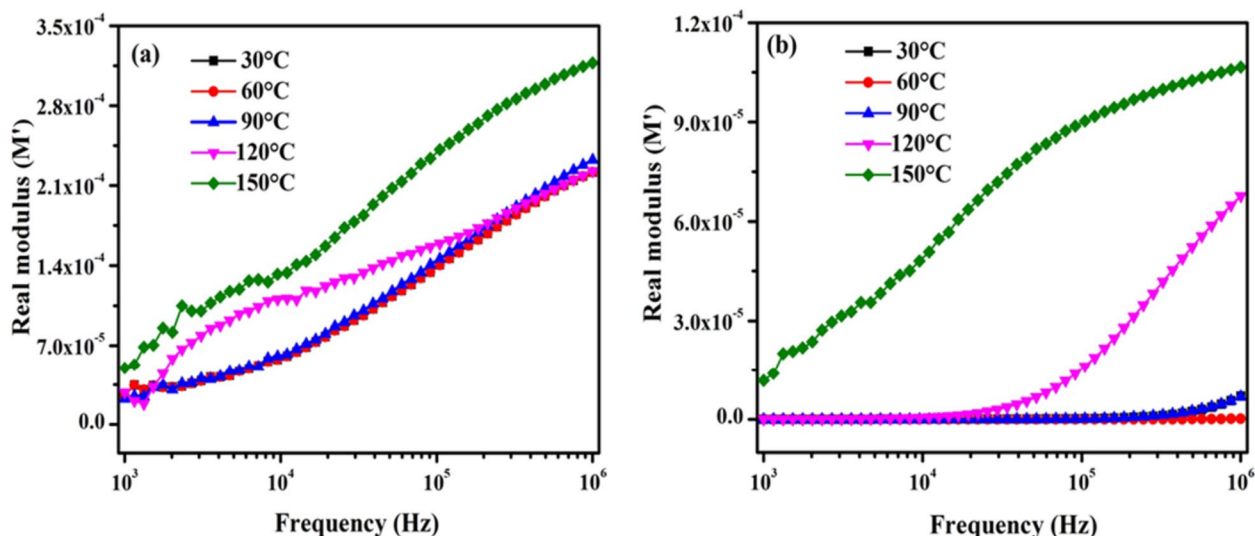
Fig. 13 Real electric modulus curves for **a** PANI–PPy and **b** PANI–ZnO–PPy nanocomposite at different temperatures
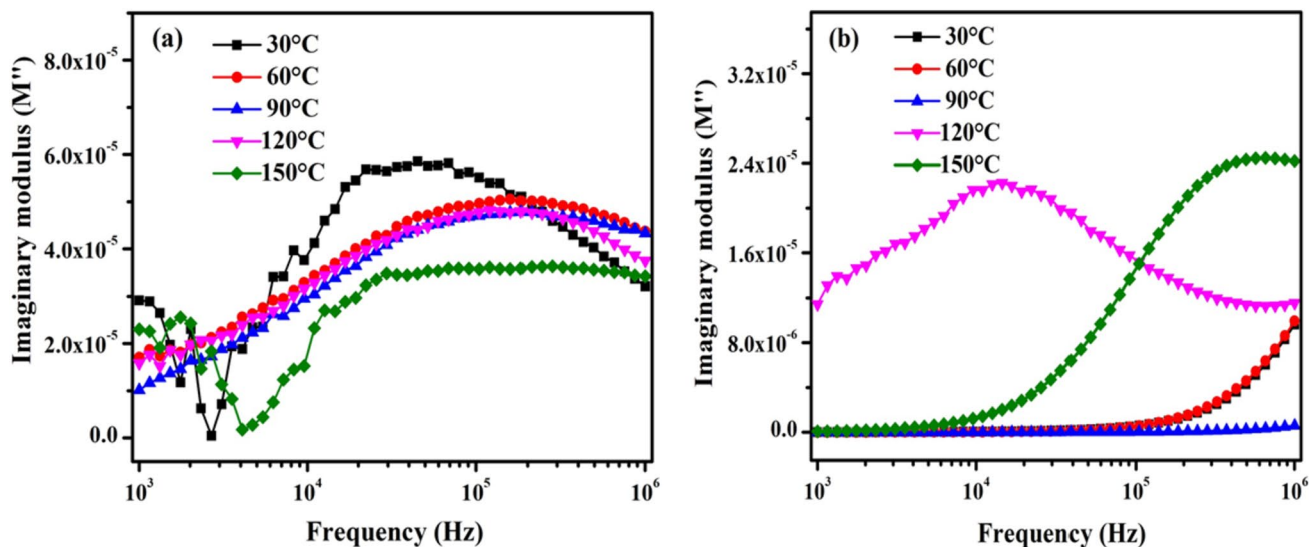

Fig. 14 Imaginary electric modulus curves for **a** PANI–PPy and **b** PANI–ZnO–PPy nanocomposite at different temperatures

the polymeric network that has facilitated fast migration of ions between PANI–PPy and ZnO.

The variation of the imaginary component of electric modulus (M") for both PANI–PPy and PANI–ZnO–PPy as a function of frequency (1 kHz to 1 MHz) and temperature (30–150 °C) is illustrated in Fig. 14a, b. The M" value gradually increases with frequency and reaches maximum at resonant frequency and beyond this frequency, M" value is found to decrease. The M" values of binary and ternary nanocomposites mostly exhibit single relaxation band around 10^4–10^6 Hz. However, the deviation is observed in PANI–ZnO–PPy within a temperature range

of 30–90 °C. In general, the relaxation peaks are shifted towards the higher frequencies with increasing temperature, which causes the decrease in relaxation time. Similar behavior is expected and is exhibited by PANI–PPy and PANI–ZnO–PPy nanomaterials as a result of fast charge carrier hopping [56]. The maximum values of M" for binary and ternary nanocomposites are found as 3.3752×10^{-5} and 2.464×10^{-5}, respectively. Similar to real electric modulus, the imaginary electric modulus of ternary PANI–ZnO–PPy exhibits low value when compared to binary PANI–PPy. This is primarily due to the grain size effect and increased hopping of ions in the ternary nanocomposite. The low values of M′ and M" and the high

values of ε' and ε'' exhibited by the ternary material goes in accordance with complex electrical modulus being the inverse of complex dielectric permittivity. Thus, the analysis of electrical modulus measurements further validate the dielectric properties of both the binary and ternary nanocomposites.

4 Conclusion

An effort is made to comprehend the optoelectronic characteristics of ternary PANI–ZnO–PPy nanocomposite synthesized through in situ oxidative polymerization process. The XRD pattern reveals the semi-crystalline phase of ternary nanocomposite due to the influence of ZnO in PANI–ZnO–PPy. The homogeneous integration of ZnO, PANI and PPy in the morphological images of PANI–ZnO–PPy indicates the successful polymerization of polymer matrix around inorganic nanoparticles. The presence of C, N, Zn and O elements in the polymer nanocomposite is confirmed by EDAX analysis. The thermal stability is studied to ascertain the ternary material's suitability for optoelectronic devices in a composite environment where a temperature change is anticipated. The calculated bandgap energy for PANI–ZnO–PPy is found to be 2.92 eV, which is lower than ZnO (3.34 eV). The low optical bandgap value is attributed to the occurrence of new localized states because of the effective interaction between PANI, ZnO and PPy in the ternary nanocomposite. The dielectric parameters namely dielectric constant (1.453×10^8), dielectric loss (6.33×10^3) and tangent loss (12.1234) are found to be highest for PANI–ZnO–PPy (frequency: 10^6 Hz, temperature: 150 °C) in comparison with binary PANI–PPy. The high AC conductivity value exhibited by PANI–ZnO–PPy (5.5767 S cm^{-1}) in comparison to PANI–PPy (2.5255 S cm^{-1}) is owing to the strong interfacial interactions between PANI, PPy and ZnO. The real electric modulus M′ (1.0703×10^{-4}) of PANI–ZnO–PPy exhibits lower value in comparison with binary PANI–PPy (3.2307×10^{-4}) due to the fast migration of charge carriers between the polymer matrix and nanofiller, which eventually improved the electrical properties. The lower band gap and the significant thermal stability suggests that the synthesized ternary PANI–ZnO–PPy nanocomposite has the potential to be employed in optoelectronic devices not only at ambient room temperature but also in an environment with fluctuating temperature.

Declarations

References

1. R. Gangopadhyay, A. De, Chem. Mater. **12**, 608–622 (2000)
2. R. Devi, K. Tapadia, T. Kant, A. Ghosale, K. Shrivas, I. Karbhal, T. Maharana, New J. Chem. **44**, 13446–13457 (2020)
3. Y. Yan, G. Yang, J.L. Xu, M. Zhang, C.C. Kuo, S.D. Wang, Sci. Technol. Adv. Mater. **21**, 768–786 (2020)
4. V.A. Scarlatache, M. Ursan, R.C. Ciobanu, 12th International Conference on Optimization of Electrical and Electronic Equipment IEEE,208–213 (2010)
5. S. Murugavel, M. Malathi, Mater. Res. Bull. **81**, 93–100 (2016)
6. A.K. Himanshu, S.K. Bandyopadhayay, R. Bahuguna, D.K. Ray, T.P. Sinha, AIP Conference Proceedings, American Institute of Physics, 1349, 204–205 (2011)
7. S.A. Saafan, M.K. El-Nimr, E.H. El-Ghazzawy, J. Appl. Polym. Sci. **99**, 3370–3379 (2006)
8. P.L. Reddy, K. Deshmukh, K. Chidambaram, M.M.N. Ali, K.K. Sadasivuni, Y.R. Kumar, R. Lakshmipathy, S.K. Pasha, J. Mater. Sci. Mater. Electron. **30**, 4676–4687 (2019)
9. N.V. Blinova, J. Stejskal, M. Trchová, J. Prokeš, M. Omastová, Eur. Polymer J. **43**, 2331–2341 (2007)
10. A.N. Papathanassiou, J. Grammatikakis, S. Sakkopoulos, E. Vitoratos, E. Dalas, J. Phys. Chem. Solids **63**, 1771–1778 (2002)
11. K. He, C. Qin, Q. Wen, C. Wang, B. Wang, S. Yu, C. Hao, K. Chen, J. Appl. Polym. Sci. **135**, 6289 (2018)
12. D. Kaur, A. Bharti, T. Sharma, C. Madhu, Int. J. Opt. (2021). https://doi.org/10.1155/2021/9950202
13. S. Pervaiz, N. Kanwal, S.A. Hussain, M. Saleem, I.A. Khan, J. Polym. Res. **28**, 1–13 (2021)
14. P.K. Singh, M.S. Gaur, R.S. Chauhan, J. Therm. Anal. Calorim. **122**, 725–740 (2015)
15. F. Majid, M. Bashir, I. Bibi, A. Raza, S. Ezzine, N. Alwadai, M. Iqbal, J. Market. Res. **18**, 4019–4029 (2022)
16. T. Debnath, S. Das, D. Das, S. Sutradhar, J. Alloy Compd. **696**, 670–681 (2017)
17. M. Purica, E. Budianu, E. Rusu, M.A. Danila, R. Gavrila, Thin Solid Films **403**, 485–488 (2002)
18. Ö.A. Yıldırım, C. Durucan, J. Alloy Compd. **506**, 944–949 (2010)
19. M. Hasanpoor, M. Aliofkhazraei, H.J.P.M.S. Delavari, Procedia Mater. Sci. **11**, 320–325 (2015)
20. H.R. Ghaffarian, M. Saiedi, M.A. Sayyadnejad, A.M. Rashidi, (2011)
21. A. Verma, R.B. Choudhary, J. Inorg. Organomet. Polym Mater. **29**, 444–455 (2019)
22. B.C. Sridhar, M.V.N. Ambika Prasad, J. Adv. Phys. **6**, 76–79 (2017)
23. P. Elumalai, J. Charles, Polym. Int. **72**, 176–188 (2023)

24. T.K. Vishnuvardhan, V.R. Kulkarni, C. Basavaraja, S.C. Raghavendra, Bull. Mater. Sci. **29**, 77–83 (2006)

25. M.R. Safenaz, M. Sheikha, Adv. Mater. Phys. Chem. (2012). https://doi.org/10.4236/ampc.2012.22013

26. H. Mi, X. Zhang, X. Ye, S. Yang, J. Power Sources **176**, 403–409 (2008)

27. V. Shalini, M. Navaneethan, S. Harish, J. Archana, S. Ponnusamy, H. Ikeda, Y. Hayakawa, Appl. Surf. Sci. **493**, 1350–1360 (2019)

28. A. Gordeeva, Y.J. Hsu, I.Z. Jenei, P.H. Brant Carvalho, S.S.I. Imak, O. Andersson, U. Häussermann, ACS Omega **5**, 17617–17627 (2020)

29. F. Paraguay-Delgado, L.A. Hermida-Montero, J.E. Morales-Mendoza, Z. Durán-Barradas, A.I. Mtz-Enriquez, N. Pariona, RSC Adv. **12**, 9898–9908 (2022)

30. S. Fu, Z. Sun, P. Huang, Y. Li, N. Hu, Nano Mater. Sci. **1**, 2–30 (2019)

31. M.J. Mochane, S.I. Magagula, J.S. Sefadi, E.R. Sadiku, T.C. Mokhena, Crystals **10**, 612 (2020)

32. M. El Rhazi, S. Majid, M. Elbasri, F.E. Salih, L. Oularbi, K. Lafdi, Int. Nano Lett. **8**, 79–99 (2018)

33. H. AlFannakh, S.S. Arafat, S.S. Ibrahim, Sci. Eng. Compos. Mater. **26**, 347–359 (2019)

34. S. Mohan, M. Vellakkat, A. Aravind, U. Reka, Nano Express **1**, 030028 (2020)

35. S. Hajiashrafi, N.M. Kazemi, Heliyon **5**, e21592 (2019)

36. T. Sahoo, M. Kim, J.H. Baek, S.R. Jeon, J.S. Kim, Y.T. Yu, C.R. Lee, I.H. Lee, Mater. Res. Bull. **46**, 525–530 (2011)

37. A.K. Zak, W.A. Majid, M.R. Mahmoudian, M. Darroudi, R. Yousefi, Adv. Powder Technol. **24**, 618–624 (2013)

38. Y. Lv, L. Wang, T. Liu, H. Liu, K. Lv, Y. Zhang, J. Wu, Energy Rep. **8**, 405–411 (2022)

39. M. Maruthapandi, A. Saravanan, J.H. Luong, A. Gedanken, Polymers **12**, 1286 (2020)

40. P.R. Jubu, F.K. Yam, V.M. Igba, K.P. Beh, J. Solid State Chem. **290**, 1576 (2020)

41. S. Saleem, M.H. Jameel, A. Rehman, M.B. Tahir, M.I. Irshad, Z.Y. Jiang, R.Q. Malik, A.A. Hussain, A. Rehman, A.H. Jabbar, A.Y. Alzahrani, J. Mater. Res. Technol. **19**, 2126–2134 (2022)

42. S. Sankar, M.T. Ramesan, Polym. Eng. Sci. **62**, 2402–2410 (2022)

43. T.A. Tikish, A. Kumar, J.Y. Kim, Adv. Mater. Sci. Eng. (2018). https://doi.org/10.1155/2018/3890637

44. A. Batool, F. Kanwal, M. Imran, T. Jamil, S.A. Siddiqi, Synth. Met. **161**, 2753–2758 (2012)

45. X. Xia, Z. Zhong, G.J. Weng, Mech. Mater. **109**, 42–50 (2017)

46. A. Azam, A.S. Ahmed, M.S. Ansari, A.H. Naqvi, J. Alloy Compd. **506**, 237–242 (2010)

47. M.E. Hajlaoui, A. Benchaabane, Z. Benhamed, N. Mahdhi, A.A. Al-Tabbakh, F. Kouki, RSC Adv. **10**, 45139–45148 (2020)

48. M.A. Almessiere, Y. Slimani, B. Unal, T.I. Zubar, A. Sadaqat, A.V. Trukhanov, A. Baykal, J. Market. Res. **9**, 10608–10623 (2020)

49. G. Zhang, D. Brannum, D. Dong, L. Tang, E. Allahyarov, S. Tang, K. Kodweis, J.K. Lee, L. Zhu, Chem. Mater. **28**, 4646–4660 (2016)

50. M. Ibrahim, A. Dawood, Egypt. J. Basic Appl. Sci. **7**, 35–46 (2020)

51. C. Rayssi, S.E. Kossi, J. Dhahri, K. Khirouni, RSC Adv. **8**, 17139–17150 (2018)

52. S. Siddabattuni, T.P. Schuman, F. Dogan, ACS Appl. Mater. Interfaces. **5**, 1917–1927 (2013)

53. S.L. Patil, S.G. Pawar, M.A. Chougule, B.T. Raut, P.R. Godse, S. Sen, V.B. Patil, Int. J. Polym. Mater. **61**, 809–820 (2012)

54. A. Maity, S. Samanta, S. Roy, D. Biswas, D. Chakravorty, ACS Omega **5**, 12421–12430 (2020)

55. S. Ahmad, I. Khan, A. Husain, A. Khan, A.M. Asiri, Polymers **12**, 3047 (2020)

56. H. Bouaamlat, N. Hadi, N. Belghiti, H. Sadki, M. Naciri Bennani, F. Abdi, T.D. Lamcharfi, M. Bouachrine, M. Abarkan, Advances in Materials Science and Engineering, 1–8 (2020)